ORIGINAL ARTICLE
International Journal of Climatology

Summertime precipitation extremes and the influence of atmospheric flows on the western slopes of the southern Andes of Perú

Elver Villalobos-Puma[1,5]* | Jose Luis Flores-Rojas[2] | Daniel Martinez-Castro[1] | Annareli Morales[3] | Waldo Lavado-Casimiro[4,5] | Kobi Mosquera-Vásquez[2] | Yamina Silva[1]

[1]Instituto Nacional de Investigación en Glaciares y Ecosistemas de Montaña (INAIGEM), Lima

[2]Instituto Geofísico del Perú (IGP), Lima

[3]National Ocean and Atmospheric Administration (NOAA), Cooperative Institute for Research in Enviromental Sciences (CIRES)-University of Colorado-Boulder, Boulder, Colorado

[4]Servicio Nacional de Meteorología e Hidrología del Perú (SENAMHI), Lima

[5]Universidad Nacional Agraria La Molina (UNALM), Programa de Doctorado en Recursos Hídricos, Lima

Correspondence
Programa de doctorado en Recursos Hídricos, UNALM, Lima, Perú
Email: 20201346@lamolina.edu.pe

Present address
*Oficina desconcentrada macro región centro, INAIGEM, Lima, Perú

Funding information
we don't have financing

Although climatologically dry, the Western Slopes of the southern Andes of Peru (WSA) can experience precipitation extremes (PEs) during the summer (December-February) resulting in great economic and human losses. Generally, WSA has a positive upslope gradient in precipitation, meaning more rain falls at higher elevations, but observations have shown this gradient can become negative with higher rainfall near the coastal cities. In this study we analyze 2000-2019 regional atmospheric patterns associated with different upslope precipitation gradients and PEs in WSA using principal component analysis methods and surface station observations. Results show important changes in the atmospheric circulation patterns during the occurrence of PE events. A prevailing pattern of negative southerly wind anomalies and regional warming of the southeastern Pacific Ocean lead to significant increases in moisture along the coast of WSA. Eastern moisture flows associated with the presence

Abbreviations: WSA, western slopes of the southern Andes of Perú; LGP , longitudinal gradient of precipitation

EVP: investigation, methodology, visualization, writing-original draft, JLFR: writing-editing, validation, formal analysis, DMC: validation, resources, methodology, investigation, AM: resources, supervision, writing–review editing, investigation, WLC: resources, supervision, investigation, KMV: resources, supervision, formal analysis, YS: project administration, conceptualization

of the Bolivian High are observed at upper levels of the atmosphere and transport water vapor from the Amazon to the western side of the Andes. Additionally, there is a blocking effect aloft in response to an intense gradient of geopotential height that attenuates the easterly circulations. These large-scale mechanisms act to concentrate high precipitable water amounts and high levels of convective available potential energy in the troposphere which favors the vertical velocities essential to trigger PEs. These results increase our knowledge of the large-scale characteristics of PEs to help with forecasting these impactful events and protecting the more than 1.8 million people living in WSA.

KEYWORDS
precipitation extremes, precipitation gradients, moisture flows, Andes, large-scale, precipitable water

1 | INTRODUCTION

The Andes Mountains extend ~7200 km along the western coast of South America, strongly influencing regional precipitation intensity and distribution. Over the southern tropical Andes (STA) the easterly zonal winds are orographically forced by the Andes resulting in dry air from subsidence processes over the western slopes of the southern Andes of Peru (WSA). This region is characterized as climatologically cold and drier compared to the eastern flank of the Andes [1, 2]. Although the transverse precipitation gradient in WSA often points west-east, i.e., less precipitation in the low zone than the high zone [2], there have been occurrences in which precipitation is concentrated in the lower and middle zones of the WSA during the austral summer, which would cause a negative precipitation gradient. These events have resulted in heavy precipitation which have produced hailstorms, floods, and landslides with strong socio-economic impacts to the 1.8 million people living in the WSA departments of Arequipa, Moquegua, and Tacna. The magnitude and direction of the precipitation gradient is critical to the WSA as it regulates the regional water system and glacial ice cover (e.g., Coropuna glacier), and thus merits further investigation on the large-scale processes influencing the precipitation gradient and associated to the heavy precipitation.

On annual and seasonal timescales, the transverse accumulated precipitation presents a positive gradient of precipitation and increases with the altitude of the topography on the WSA. This pattern can change on a daily scale, especially during the phases of El Niño Southern Oscillation (ENSO) [2, 3] more precipitation can occur on lower elevation slopes. Previous studies analyzed the variability of precipitation using indices that characterize sea conditions in different domains and time scales [4, 5, 6, 7], finding an inverse correlation between the Niño 3.4 index and WSA precipitation [4, 8]. In contrast, the correlation between El Niño 1+2 and WSA has an inverse relationship with the northern region of WSA and a direct correlation with the southern region of WSA [4]. On a regional scale, the precipitation responds to the physical processes that locally control fluctuations of sea surface temperatures (SSTs), in which low-level winds favor the upwelling and cooling of the sea along the Peruvian coast [9, 10, 11]. The intense rainfalls, which cause socio-economic impacts over WSA, do not have a defined frequency pattern associated with the phases and domains of the ENSO. These intense rainfalls can occur for different combinations of the phases (warm and cold) and the indices (3.4 and 1+2) of the ENSO. Likewise, these events can respond strictly to atmospheric forcing that induce local warming of the sea and advection of humidity in coastal areas [12], and there can also be mesoscale circulations that bring humidity to the WSA.

The WSA precipitation distribution peaks in the summer coinciding with the mature phase of the South American Monsoon [8]. In this phase, precipitation is controlled by the advection of humidity from the Amazon in accordance with the easterly winds and the Bolivian High (BH) [13, 14]. The BH generally occurs over the central Andes and can generate disturbances in the zonal flows depending on its intensity and location [15, 13]. These zonal flows exert an important influence on the precipitation in the WSA, especially during the summer, where their anomalies favor humid conditions east of WSA [16].

The other mechanism associated with the precipitation in the WSA is the convection that develops west of the Amazon in the border region with the northern central Andes [17]. This convection results in an intense humidity convergence and upward vertical motions that transport energy and momentum from low levels to higher levels of the atmosphere [18]. Additionally, the precipitation in the WSA has a positive correlation with the airmass transported by the low-level jet (LLJ) associated with the northern synoptic flows [19, 20]. The LLJ transports warm, humid air from the Atlantic Ocean in a north-south direction along the eastern flank of the Andes, channeling moisture into the inter-Andean valleys [21, 19]. The Andes exert dynamic forcing on these flows at both a local and regional scale, and in general, they intensify precipitation on the eastern slopes of the Andes and reduce precipitation to the region of the WSA [22, 23, 19].

The atmospheric circulation patterns and main sources of moisture associated with intense rainfall in WSA have not been sufficiently explored. Thus, the purpose of this study is to examine the dynamic and thermodynamic state of the atmosphere with the aim to improve the knowledge related to the precipitation gradient in the WSA region. In this study, we address the following scientific questions: 1) does the precipitation gradient change in magnitude or direction on daily scales?, 2) what large scale patterns are associated with any changes in precipitation gradient direction?, and 3) what is the source of moisture and large-scale patterns associated with intense rainfall events?

The article has the following structure. In section 2 we present the study area, the in situ precipitation and SST data, radiosonde observations and the reanalysis of synoptic circulations and atmospheric variables. Section 3 provides a description of the methodology and the moisture flux detection procedure. Section 4 presents the precipitation analysis and connections to thermodynamics and atmospheric flows. Sections 5 and 6 describe the discussion and results of this work, respectively.

2 | STUDY AREA AND DATA

This study focuses over the southern region of Peru where the department capitals of Arequipa, Moquega, and Tacna are located below 3000 m ASL (red stars in Fig. 1). These coastal cities are directly affected by the intense rainfalls during summer austral.

Daily rain gauge data was used from several stations distributed along the WSA (Figure 1). Two transects (T1 and T2) exist each one with seven stations, labeled E1, E2, E3, ..., E7 (Fig. 1). The description of the in-situ stations is shown in Table 1. Stations E1 of T1 and E1 of T2 are located in the cities of Arequipa and Tacna, respectively. The location of this set of instruments presents an advantage, since they provide information on precipitation at high elevations, where accessibility is difficult and in-situ measurements are scarce. The analysis period is 2000-2019 corresponding

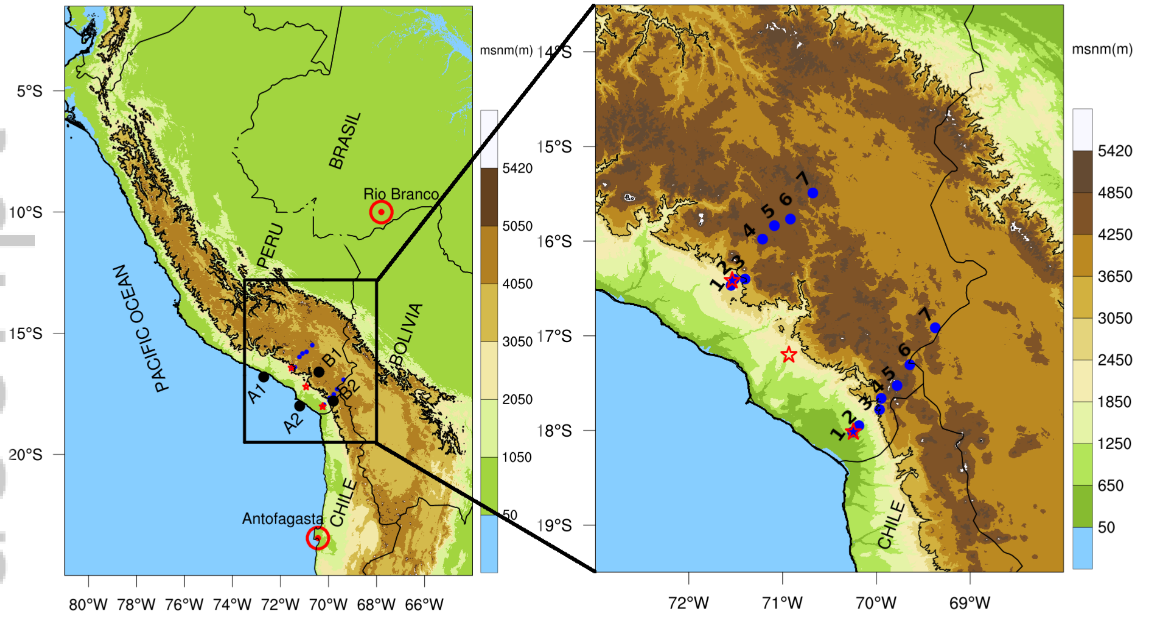

FIGURE 1 The left panel shows the countries of South America and the Andes mountain range (3000 m ASL contour in black), points A1, A2, B1 and B2 will be used as a reference to detect moisture flows. In the right panel is the study area, the red stars indicate the cities of southern Peru, from north to south; Arequipa, Moquegua and Tacna. The blue dots numbered from 1 to 7 indicate the rainfall stations distributed in a cross-section along the WSA, the north is transect 1 (T1) and the south is transect 2 (T2). Rio Branco and Antofagasta are radiosonde observation points in the left panels.

to the National Service of Meteorology and Hydrology of Peru (SENAMHI) database. Only months with more than 90% of existing data were considered. For the period 2000-2019 (60 summer months) for T1, 3 months of missing data were found in E3 and the rest of the stations have complete data. For T2, missing data were found for 7, 5, and 9 months in E3, E4 and E5, respectively, and the rest of the stations have complete data.

Daily SST data (2007-2019) with high spatial resolution (0.08 degrees) were also used, obtained from the Operational Sea Surface Temperature and Ice Analysis [24]. Radiosonde observations were taken from the Rio Branco airport in Brazil and the Antofagasta station in Chile (Fig. 1). Both stations provided data from 2004-2019. The radiosonde data was downloaded from the Integrated Global Radiosonde Archive.

For analysis of synoptic circulations and atmospheric variables, the ERA5 reanalysis dataset was used [25] from 2000-2019. ERA5 is a three-dimensional product of the European Center for Medium-Range Weather Forecasts with 31 km spatial resolution and hourly temporal resolution. The atmospheric variables used were specific humidity (g/kg), zonal and meridional wind speeds (m/s), vertically-integrated water vapor (IWV, kg/m^2), geopotential height (m), and convective available potential energy (CAPE, J/kg) used to evaluate atmospheric instability associated with convective activity in the study region [26]. Instantaneous fields of ERA5 data (14LT) were used and related to daily rainfall and SST data.

TABLE 1 Description of in-situ stations, where En is for T1 and E_n^* is for T2

	E_1	E_2	E_3	E_4	E_5	E_6	E_7
Lat(°)	-16.467	-16.403	-16.400	-15.979	-15.837	-15.767	-15.491
Lon(°)	-71.550	-71.517	-71.400	-71.214	-71.088	-70.917	-70.678
Alt (m)	2242	2400	2900	4455	4519	4470	4320
	E_1^*	E_2^*	E_3^*	E_4^*	E_5^*	E_6^*	E_7^*
Lat(°)	-18.017	-17.949	-17.779	-17.661	-17.525	-17.305	-16.915
$Lon(^\circ)$	-70.254	-70.186	-69.966	-69.949	-69.779	-69.644	-69.373
Alt (m)	560	900	2940	3620	4597	4220	3940

3 | METHODOLOGY

3.1 | Classification of precipitation gradients using orthogonal indices

Precipitation in WSA was characterized through two orthogonal indices calculated using the linear combination statistical technique, which focuses on the principal component analysis (PCA) [27]. The T index indicates the total precipitation anomaly that occurs on the transect, while the R index is associated with the variation of local precipitation between stations [27]. These orthogonal indices were proposed by [27] to quantify the rain shadow effect, and in general, to characterize the cross-sectional rainfall over a mountain range. The indices were calculated using stations E3-E7. Stations E1 and E2 were not used because the accumulated rainfall is very scarce during the summer. The precipitation data were normalized by subtracting the respective total average and dividing the respective standard deviation for each station. The methodology described below is for the T1 transect, and the same procedure applies for the T2 transect.

Table 2 shows the correlations between stations E3 to E7 for the T1 transect. The correlations are positive and each rain gauge has its own statistical significance. The correlation between the extreme stations (E3 and E7) is 0.16. This low correlation may be caused by the diurnal cycle of atmospheric circulations that are associated with localized rainfall in the inter-Andean valley [19].

The quantification method consists of the weighted sum (E_n^*) of stations of each transect, using the normalized precipitation data of the stations E3 and E7:

$$E_n \approx E_n^* = \alpha_n E_7 + \beta_n E_3 \tag{1}$$

Where, E_n represents the normalized precipitation data (E_n, where n = 3,4,5,6,7) and E_n^* represents the linear combination described in Eq. 1. The alpha and beta coefficients were determined using ordinary least squares regression (Table 3). The correlations between E_n and E_n^* have a moderate level of significance.

After verifying the moderate statistical significance of the correlation between E_n and E_n^*, the orthogonal indices T and R are constructed:

TABLE 2 Pearson's correlation coefficient between the rain gauges for the T1 transect

$T1$	E_3	E_4	E_5	E_6	E_7
E_3	1				
E_4	0.40	1			
E_5	0.33	0.52	1		
E_6	0.27	0.43	0.60	1	
E_7	0.16	0.27	0.32	0.29	1

TABLE 3 Pearson's correlation coefficient between E_n and E_n^* for summer precipitation

	E_3^*	E_4^*	E_5^*	E_6^*	E_7^*
$Corr(E_n^*, E_n)$	1	0.42	0.41	0.33	1
α	1	0.324	0.251	0.203	0
β	0	0.208	0.276	0.222	1

$$T = E_7 + E_3 \tag{2}$$

$$R = E_7 - E_3 \tag{3}$$

Table 4 shows the correlation coefficients between R and E_n^*. The highest correlations are +0.65 and −0.64, indicating a significant variation in precipitation along the T1 transect. This local variation is explained at 41% by R and the remainder is explained by T. However, the correlation coefficients are low for stations (E_4^*, E_5^* and E_6^*), indicating there is no significant difference in the magnitude of rainfall between these stations.

To characterize the cross-sectional variation in precipitation, the R index values were classified into low, medium, and high subgroups. Low values represent a negative gradient (NG), values close to zero are neutral (Neu) and high values represent a positive gradient (PG). In addition, to understand the cross-section of precipitation, the frequency precipitation (Pf) and intensity precipitation (Pi) were defined. Pf is a fraction between the number of days with rain and the total number of days multiplied by 100. Pi is the precipitation rate per unit of time, in this case mm/day is used due to data availability. Precipitation extremes (PEs) represent precipitation values greater than the 95th percentile of the data. This criterion was applied preferentially to stations E3 and E4, as these are located below 3000 m ASL in the WSA. The cross-sectional accumulated precipitation from events classified as PG, NG, Neu and PE define the longitudinal gradient of precipitation (LGP) patterns on the WSA. Analyses were performed for the wet season (November-April) and summer (December-February)

TABLE 4 Correlation coefficients (R) between R and E_n^*, and R^2 is the statistical significance for T1

	E_3^*	E_4^*	E_5^*	E_6^*	E_7^*
R	0.65	0.20	-0.02	-0.01	-0.64
R^2	0.43	0.04	0.0	0.0	0.41

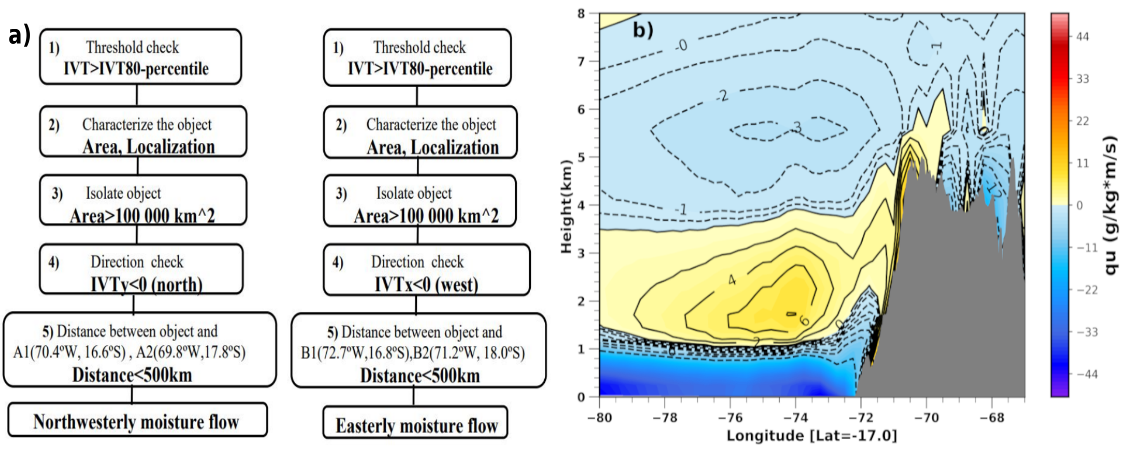

FIGURE 2 a) Procedure to identify northwesterly moisture flow (NWMF) and Easterly moisture flow (EMF), points A1, A2, B1 and B2 (see in Figure 1). b) Horizontal flow climatology, height versus longitude (cross-section at latitude: -17° S). Positive values are flows from the west and negative are flows from the east.

3.2 | Detection of atmospheric fluxes

Two atmospheric layers were used to identify atmospheric moisture fluxes, 650 hPa to 200 hPa and 800 hPa to 875 hPa. These layers were selected using the 2000-2019 wind climatology from ERA5 reanalysis. The integrated water vapor transport (IVT) was then calculated for both layers and labeled as IVT1 and IVT2:

$$IVT_1 = -\frac{1}{g}\int_{650hPa}^{200hPa} qUdp, \quad IVT_2 = -\frac{1}{g}\int_{800hPa}^{875hPa} qUdp \tag{4}$$

where, U represents horizontal wind speed, q is specific humidity and p is pressure. IVT_1 (kg*m^{-1}*s^{-1}) is the vector field of the moisture flow entering the WSA from the eastern inter-Andean valleys, hereinafter referred to as the easterly moisture flow (EMF). IVT_2 (kg*m^{-1}*s^{-1}) represents the northerly flow of humidity off the Peruvian coast, hereinafter referred to as the north-westerly moisture flow (NWMF). The range of pressure levels in equations 1 and 2 were selected using the flow climatology, which was calculated with the 2000-2019 ERA5 reanalysis data. Below 875 hPa, the winds are southerly due to the influence of the South Pacific anticyclone, while above 800 hPa the winds are influenced by the EMF. In Figure 2a, two flow regimes are observed over the Pacific Ocean, which is the reason for considereig the two levels of IVTs (IVT1 and IVT2).

The identification process of both moisture flows is shown in Figure 2a. The magnitude of the IVT was first verified using a local threshold equal to its 80th percentile. The 80th percentile was applied to the complete IVT series (2000-2019) for each month and at each grid point of the ERA5 reanalysis. The calculation was for 14 LT, because this time is consistent with the formation of cold clouds and rainfall that occur in the afternoon in the STA [28]. IVTs were then characterized as a geometric object based on area and location, specified in steps 2 and 3 of Figure 2a. The areas threshold was 100,000 km^2 and the direction was verified using IVTs entering the WSA region. The geometric objects must exist within a radius of 500 km around points A1, A2, B1 and B2 located within the WSA, specified in step 5 of Figure 2. The EMF and NWMF extends like a jet of moisture in the tropics, for its quantification an elongated 5°x2° grid ($\approx$ 100000 km^2) domain of IVT was considered. On the other hand, sometimes the flows do not reach points A1, A2, B1 and B2 (see in Fig. 1), but they are important because they transport moisture to the region. Therefore, to guarantee the detection of the flows, a relatively short distance of 500 km was used. For example, those NWMF that passed near the coast of Peru could be detected by the algorithm. Figure 2b shows the climatology cross-section of the zonal flow. The zonal flow has a different regime in the middle of the troposphere over the ocean and western slopes of the Andes, this atmospheric layer (yellow outline) was used to identify the NWMF and above it was used to identify the EMF.

4 | RESULTS

4.1 | Cross-section of precipitation at different time scales

Average annual precipitation (Figs. 3a, b) shows a significant longitudinal gradient over the WSA region, i.e., the areas near the coast are drier than the high-Andean regions. For T1, the annual rainfall in the E1 station (2.7 km ASL) is approximately 11 cm/year and the E7 station (4.8 km ASL), located 200 km from the Pacific Ocean, is 82 cm/year (Fig 3a). Similarly, for T2 (Fig. 3b), the annual precipitation increases from the areas near the coast towards the high-Andean areas.

During both the wet season and summer season, the contribution to annual precipitation for both T1 and T2 has an inverse relationship with elevation. For T1, the contribution to annual precipitation during the wet season (summer season) is 90% (60%) at high elevations and 100% (80%) near the coast (Fig. 3a). For T2, from station E3 to station E7, the transverse contribution has the same pattern as at T1. However, in the stations near the coast (E1 and E2), the contribution to annual precipitation has a different pattern. In these stations, during the summer there is a contribution of 20% and during the wet season of 30%. This means that 70% of the small amount of annual precipitation that accumulates at E1 and E2 corresponds to May-October.

These results confirm that LGP is positive (West-East) on an annual and seasonal scale (Figs. 3a, b). However, when the LGP is calculated at daily time scales using the R index (see section 3), LGP can be positive and negative as shown in Figs. 3c and 3d. The LGPs with a positive direction (black whiskers) have a clear pattern during the wet season that begins in November and ends in April, and their peak is centered on the months of January and February. In both transects (T1 and T2) there is a strong positive gradient that can increase on average up to 4 (mm/km)/month in critical months (January-February). The negative LGP (blue whiskers) presents significant values in the months of January and February and lasts until March. This result shows that the LGP changes drastically in the summer months (December-February), therefore, the rainfall during this period will be studied in greater detail.

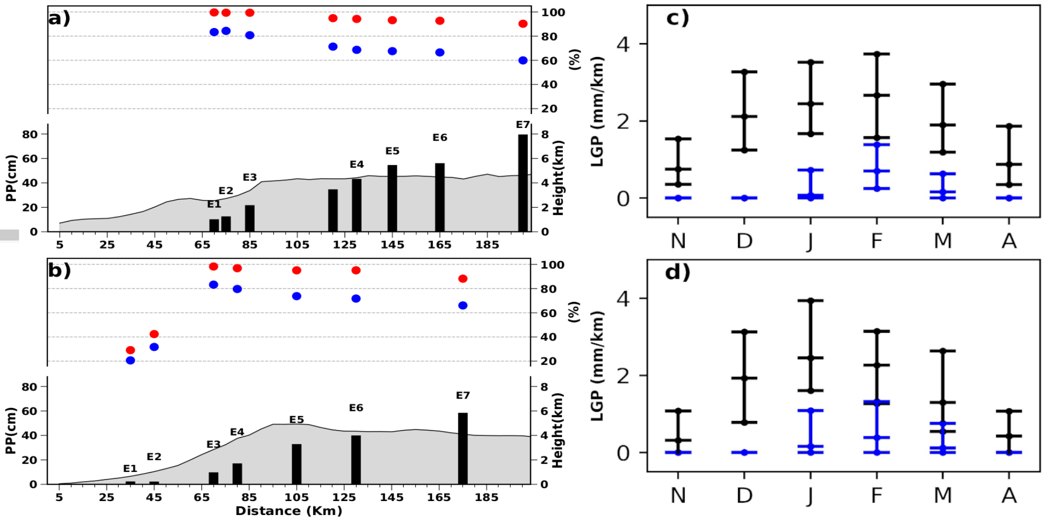

FIGURE 3 Average annual precipitation (PP, black bars) calculated at each station (E1, E2, E3,..., E7), the contributions (%) to the annual precipitation during the wet period (Nov-April) are denoted with red circles and summer (December-February) are denoted with blue circle. a) Arequipa transect (T1), b) Tacna transect (T2). The right column shows the average LGP expressed in (mm/km)/month and determined for stations E3-E7, black when the LGP is positive and blue when the LGP is negative. c) T1 transect and d) T2 transect. In both transects the lower, central and upper whiskers are 25th, 50th and 75th percentiles, respectively.

4.2 | Cross-sectional precipitation during different LGP patterns and PEs

Figure 4 shows the accumulated precipitation (PP), the frequency (Pf) and the intensity (Pi) for the negative gradient (NG), positive gradient (PG) and neutral (Neu) events. During the PG events (Fig. 4a), the values of Pf and Pi vary considerably from west to east. It is observed that Pf increase from 25% to 100%, and Pi increase from near zero at the coastal stations to 18 mm/day (75th percentile). The transversal variation of the accumulated precipitation responds to the variation of both Pf and Pi. Consequently, PP increase from 0.05 m to 7.2 m with a LGP rate of +8.4 (mm/km)/month. It is evidenced that PG events are more intense in regions east of the WSA and contribute 78% to the total summer precipitation and in the lower regions of the WSA contribute 12% during the same summer season. The NG events are shown in Fig. 4b. The transversal accumulated precipitation of these events has a different pattern in relation to those of the PG type. The gradient of these events is negative and on average the LGP decreases at a rate of -1.6 (mm/km)/month in the east-west direction. This decrease can be explained in terms of Pi and Pf. The Pi for the station near the coast presents important variations of its quartiles, whose 75th percentile exceeds the value of 6 mm/day. However, the Pi presents a smaller 75th percentile equal to 1 mm/day for the station on the higher slopes. Likewise, the Pf has a moderate transverse variation that decreases in the west-east direction. The increase in PP towards the west is a consequence of the variations in Pi and Pf, although it is observed that Pi is more influential than Pf to changes in PP. The NG events are important near the coastal areas, because they contribute 82% of the accumulated precipitation during the summer months (Fig. 4b).

For Neu events (Fig. 4c), the transverse variation of the PP is low and these events are associated with light precipitation that occurs across T1. For PE events, it is clearly observed that the transversal variation of Pi is more significant than Pf (Fig. 4d), where the 75th percentile reaches values of 20 mm/day in the station at lower slopes

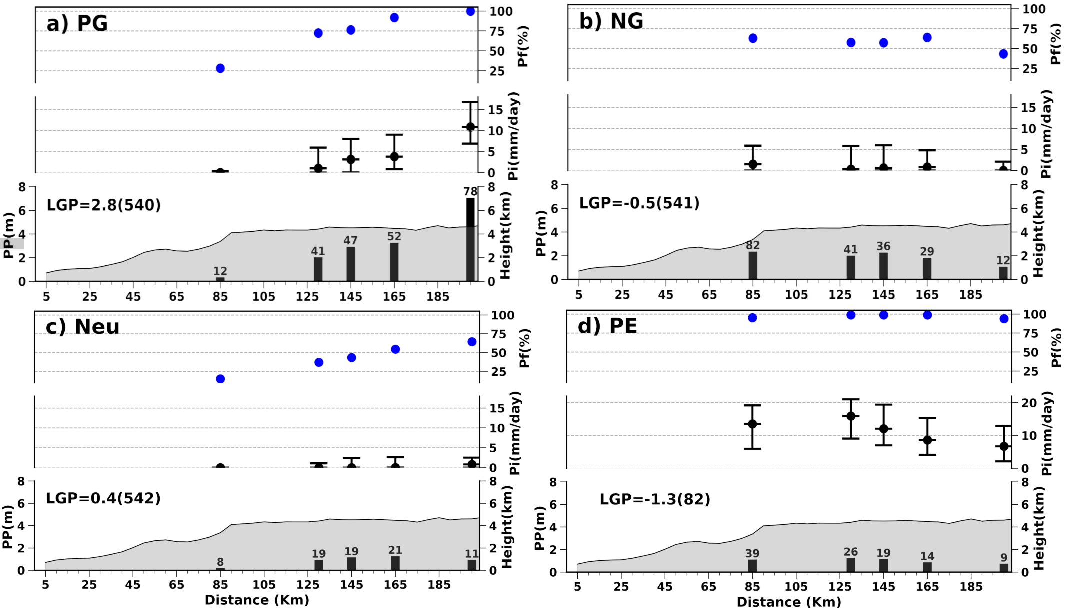

FIGURE 4 Accumulated precipitation (m, black bars), intensity (mm/day, black barbs) and frequency (%, blue points) for the precipitation events classified in a cross-section way on the T1: a) Positive gradient (PG), b) Negative gradient (NG), c) Neutral (Neu) and d) Precipitation Extreme (PE). The numbers above each bar indicate the relative contribution in percentage to total accumulated precipitation, the LGP[(mm/km)/month] is west-east (+) and east-west (-), and the number in parentheses indicates the number of event cases. In all panels the lower, middle and upper whiskers are 25th, 50th and 75th percentiles, respectively.

of WSA. These precipitation intensities are quite high for this region. For T1, 82 PE events were found in 2000-2019, which on average represent 4 events per summer, and for T2, 77 PE events were found. The black bars Fig. 4) represent the accumulated precipitation of all the events that met the PE and NG criteria (noted in section 3). In total, 541 NG events and 82 PE events were found. It is expected that the greater the number of events, the greater the accumulation of precipitation. Therefore, in terms of accumulated precipitation NG events have larger magnitudes than the PE events (compare Fig 4b and d). Although fewer PE events occur, those few events are extremely intense compared to the intensities of other PG and NG events.

The spatial pattern of accumulated precipitation on a monthly and annual scale shows a positive gradient [2]. From the R index that adequately characterizes the transversal rainfall, it was evidenced that it is important to choose an adequate time scale to quantify the variation in precipitation along transects in the Andean areas. This is due to the fact that for the annual and seasonal scale there is a positive gradient and for daily scales negative gradients can be found, such as the NG and PE events.

4.3 | Atmospheric circulation patterns associated with PG, NG and PE events

4.3.1 | Moisture flows and geopotential height anomaly

The moisture flow and the geopotential height anomaly are shown in Figure 5. At 950-hPa the flows associated with the PG events are characterized by the fact that in the Pacific Ocean the transport of water vapor increases between latitudes 5°S and 25°S in relation to the NG and PE events (Fig. 5c). The anomaly of the geopotential height does not show significant variations for the PG, but does show changes in anomalies for NG and PE. Specifically for PEs, the gradient of the anomaly is more intense, which shows that the reduction of the flow of humidity is generated in response to the anomaly of the geopotential height that occurs in the lower levels of the atmosphere. The atmospheric pressure decreases significantly during the PE events over the South Pacific and in the North Pacific Ocean it increases, so this difference in atmospheric pressure conditions favors the transport of water vapor. The results are consistent with the specific radiosonde observations of Antofagasta (Figs. 6a and b), in which it is observed that the anomalies at 1000 hPa are negative and the temperature anomalies are positive for the PEs. This means that the wind in the south weakens as the air temperature increases in relation to its average climatology (Fig. 6a).

At 850-hPa,on the Pacific Ocean off the Peruvian coast moisture is transported in a north to south direction. In these regions there are important differences between the magnitudes of the moisture transport depending on the types of events. For the NG events (Fig. 5e) off the coast of Peru, there is a slight increase in the magnitude of moisture flow, this increase is more noticeable for the PE events. Moisture flows spread like a plume from the coastal region of northern Peru to the south (20°S) parallel to the coast, which manages to connect with the coastal region of WSA (Fig. 5f). These humidity flows are characterized by having a positive temperature anomaly equal to 0.12°C and a higher humidity content (not shown in Fig. 6 but verified using the radiosonde data from the Lima airport). The increase in moisture transport is driven by the difference in geopotential height that occurs at this level of the atmosphere, where the south presents negative anomalies and the north positive anomalies (Fig. 5c). This pattern is observed at 950-hPa and 850-hPa, but at 850-hPa the transport of water vapor occurs in the opposite direction (north-south) and its magnitude is more pronounced off the Peruvian coast (Fig. 5f). Likewise, in the eastern Andes there are differences in the magnitude of the humidity flows for the three types of events. It is observed that between the latitudes of 10°S and 15°S on the borders of Peru and Bolivia the moisture transport is considerably weakened during PE events (Fig. 5f).

At 500-hPa, the weak moisture fluxes prevail in the northeast direction for the PG and NG events over the WSA region, while, for the PE events, the magnitude of the moisture flux increases, and its direction is more perpendicular to the Andes (Fig. 5i). In turn, a negative anomaly of geopotential height occurs over the WSA region (Fig. 5i), showing that during these events a low pressure is produced in relation to its climatology. The pressure configuration conditions the confluence of the moisture fluxes exactly over the WSA region and its coastal region. Radiosonde observations at Rio Branco indicate that the airmass that enters the Andes has negative anomalies of air temperature and dew point depression (Figs. 6e, g). That is, the air transported is colder and with more moisture content than normal, especially during PEs. This same pattern is observed on the north coast of Chile (Antofagasta), the moisture content prevails, but the environment is warmer than normal (Figs. 6a, c), which indicates that the air over the coast has more capacity of storing water vapor.

At 200-hPa, the position of the geographic center of BH is well located for the three types of events (Fig. 5). For PG events, the geographic center of the BH is located exactly over Bolivia and for the NG events (Fig. 2b), the center of the BH persists and the gradient of the geopotential height anomaly increases slightly towards the south. For PE events, the gradient of the geopotential height anomaly is more intense and the center of high pressure of the BH is well defined and positioned further south compared to other types of events. From the Antofagasta radiosonde it is observed that 500-200 hPa for PE events, the atmospheric structure has positive anomalies in temperature and geopotential height, and negative anomalies in horizontal wind and dew point depression (Fig. 6). These anomalies indicate that the air is hotter than normal and with a higher moisture content, which generates an increase in atmospheric pressure. In addition, the horizontal wind weakens in response to the strong gradient of the geopotential height anomaly.

4.3.2 | Precipitable water and CAPE

The IWV anomaly (Fig. 7a) is neutral for PG events, being consistent with the result of the IVT anomaly (Fig. 7d). In addition, the water vapor transport anomaly does not show a significant change in relation to its climatology over the WSA area. In contrast, the CAPE anomaly (Fig. 7g) is more pronounced over the altiplano region. This shows that PG events are associated with convective activity that occurs mainly in the highlands. For NG events, the positive IWV anomaly is most pronounced in the southeastern Pacific Ocean and over the region near the WSA coast. This positive pattern of the IWV anomaly is explained by the positive IVT anomaly that predominates over the Pacific Ocean. Positive water vapor transport anomalies are associated with the increase in IWV anomalies during NG events. Likewise, the CAPE associated with this type of event presents a narrow strip along the Pacific slope, it is displaced towards the west in relation to the PG events. This result indicates that the convective activity is located to a greater extent over the WSA region.

The PE events are distinct because they present an intense positive anomaly of the IWV and these are located to the south of the eastern Pacific Ocean and over the WSA region. This pattern is associated with the positive anomaly of the IVT (Fig. 7c), which extends like a feather off the coast of Peru and northern Chile. This shows that the moist flow from the north has an important role in the transport of water vapor, which is consistent with the moist flow from the north that was observed at 850-hPa (Fig. 5) and increased locally off the Peruvian coast. In contrast, the opposite occurs in the Amazon region east of the Andes. The magnitude of the anomalies of the moist flow are negative, while, in the interior of the Andes (between Peru and Bolivia) they are positive due to the intensification of the eastern flow that enter the Andes, specifically in the middle and upper levels of the atmosphere (Fig. 5i). In turn, the CAPE (Fig. 7c) shows positive anomalies on the Pacific slope, especially over the WSA region, where the anomalies exceed their climatological average by more than 350 J/kg.

4.3.3 | Sea conditions, south wind and moisture fluxes

During PG events (Fig. 8a), the SST anomaly has values close to 0° C, this means that it does not differ significantly from its climatological value. For NG and PE events, a well-defined positive SST anomaly is observed (Figs. 8b and c). For PE events, the positive SST anomaly is more intense and extends as a warm pool between latitudes 7° S and 25° S off the coast of Peru and northern Chile. This warm pool has a very important frequency of occurrence that ranges between 50% and 60% (Fig. 8a), in addition, to the presence of positive SST anomalies, weak winds from the south are observed (Fig. 8b). This weakening of the south winds has a well-defined spatial pattern with frequencies that vary between 70% and 80% of occurrence over the Pacific Ocean south of Peru and north of Chile. Both atmospheric and ocean conditions regionally control the increase in humidity at low levels of the atmosphere off the southern Peruvian coast (Fig. 8f). Over the same region an intense positive anomaly of specific humidity is observed at levels close to the surface that represents more than 90% of all PE events. These results show that the WSA region is favored by a significant increase in specific humidity that is concentrated locally during the occurrence of PE events.

Figure 9 shows the averages of IVT1 and IVT2 associated with the occurrence of PG, NG and PE events. For PG events there is a flow over the Pacific Ocean that transports water vapor in a north to south direction and has the shape of a plume that extends south parallel to the Peruvian coast (Fig. 5a). For the other types of events (NG and PE), this plume is more pronounced (Figs. 9b and c). For PE events, the plume has the shape of an atmospheric jet that contains a large amount of water vapor and manages to reach the north of Chile (23°S). Likewise, during this type of event there is a significant connection between the north and south of Peru characterized by their high temperature and high moisture content at low levels of the atmosphere (875-800 hPa). This flow likely plays an important role during the warm phase of the eastern Pacific Ocean and may favor the occurrence of convective processes in the WSA region.

In the middle to upper levels of the atmosphere, the IVT2 pattern is different (Fig. 9d, e and f). For PE events, the moisture flows tend to be more perpendicular to the Andes and their magnitude also increases over the regions between the border of Peru and Bolivia. In general, a significant increase in the flow of water vapor from the Amazon is observed in the interior of the Andes, which increases the specific humidity and IWV concentration over the WSA region (Fig. 9f).

To evaluate the spatial pattern of water vapor transport associated with PE events, the frequency of the positive IVT anomaly in three atmospheric layers was determined. The IVT_sfc (Fig. 9g) was calculated at levels close to the surface (975-950 hPa), while IVT1 (Fig. 9b) and IVT2 (Fig. 9c) were already defined in the methodology section. The IVT_sfc has a significant frequency of occurrence (between 60 and 70%) and its spatial pattern is concentrated in the southern region off the coast of the WSA region, which is consistent with the high intensity of the positive SST anomaly (Fig 8c). In addition, IVT1 shows frequencies of occurrence with high percentages (between 70 and 80%) in extensive regions on the southern Pacific Ocean, due to the fact that at these levels the flow of moisture moves like a plume from the north to the south of Peru. For IVT2 there is also a high frequency of occurrence (between 60 and 70%) driven by flows from the east and located over the WSA region. These results show that moisture fluxes play an important role in the three atmospheric levels and are responsible for the generation of extreme precipitation in the WSA region.

4.4 | Impact of atmospheric flows on precipitation

The moisture flow of NWMF and EMF were identified based on IVT1 and IVT2 (Figs. 9c and f), respectively. 1139 NWMF fluxes and 819 EMF fluxes were identified during the summer seasons (December-February) in the period 2000-2019. The average of both flows (NWMF and EMF) is shown in Figure 10, where it is observed that the pattern of the spatial distribution of both is like the average of the IVT1 and IVT2 flows for the PE events (Fig 9c and 9f, respectively). In particular, the EMF flow (Fig. 10b) presents a vector field that enters perpendicular to the WSA region. These results demonstrate the efficiency of the algorithm used for the identification of the NWMF and EMF flows. The average frequency of both flows (NWMF and EMF) during the summer seasons of the study period are shown in Figures 10c and 10d, respectively. It is observed that the NWMF on average occurs between 15 and 17 times in each summer and they are mainly located off the southern Peruvian coast. While EMF flows on average occurs between 9 and 11 times in each summer and are mainly located in the interior of the central Andes.

Figures 11a and 11b show the fraction of precipitation associated with the presence of NWMF for the T1 and T2 transects, respectively, which vary according to the summer season considered. For the T1 transect, the minimum fraction is 51% in 2003 and maximum 90% in 2017. On average, the fraction of precipitation associated with NWMF was 69% in the period 2000-2019. For PE events it was found that the number of cases associated with the presence of NWMF flows was 77, which represents 81% of all PE events. For the T2 transect, the minimum fraction is 50% in 2002 and the maximum 91% in 2017. On average, the fraction of precipitation associated with NWMF was 68% in the period 2000-2019. For PE events, it was found that the number of cases associated with the presence of NWMF flows was 82, which represents 75% of all PE events. Figures 11c and 11d show the fraction of precipitation associated with the presence of EMF fluxes for the T1 and T2 transects, respectively. For the T1 transect, the minimum fraction is 33% in 2007 and maximum is 77% in 2006. On average, the fraction of precipitation associated with EMF was 58% in the period 2000-2019. It was found that EMF flow is associated with 63% of all PE events that occur in T1. For the T2 transect, the minimum fraction is 37% in 2002 and the maximum is 78% in 2013. On average, the fraction of precipitation associated with EMF was 59% in the period 2000-2019. It was found that EMF is associated with 72% of all PE-type events that occur in T2.

To analyze the intensity of precipitation associated with moisture flows (NWMF and EMF), these fluxes were classified into three subgroups with the following criteria: when both NWMF and EMF occurred simultaneously, when only the NWMF occurred, and when only the EMF flow occurred, which will be referred to as flows of type A, B and C, respectively. The influence of flows on the intensity of precipitation is shown for each pluviometric station in Figure 12. At station E1 located 70 km from the coast and at an altitude of 2500 m ASL, it is observed that the quartiles decrease from left to right, which are associated with flows of type A, B and C, respectively. This behavior reveals that more intense events occur on lower slopes due to the presence of type A flows. On the contrary, in the other stations the influence of the moisture flows is reversed. Specifically, In the E4 station located above 4000 m ASL and 130 km from the coast towards the east, the type C flows had greater influence on the intensity of PE events, although for station E7 the most intense PE events were associated with the presence of type B flows. Furthermore, for PE events in T2 (Fig. 12), it was found that the percentage of PE events associated with the presence of type A, B and C flows have high values in relation to the T1 stations. 58% of PE events occurred in the presence of type A flows, 23% occurred in the presence of type B flows, 14% occurred in the presence of type C flows, and the remaining 5% responded to other unidentified factors.

At stations E1, E2, and E3 shown in Figure 12b, located 35, 45 and 70 km from the coast, respectively, and below 2500 m ASL, it is observed that the quartiles decrease from left to right, although the intensity is minimal at the coastal stations (E1 and E2). On the contrary, at the other stations the influence of the flows is reversed. For example, at station E7 type C flows have a greater influence on the intensity of PE events. The results of T2 are consistent with the results of T1, in which it is evident that the flows of types A, B and C exert a control over the intensity of precipitation, mainly for events of the PE type. These results show that the NWMF are associated with the intensity of the PE events in the stations located in the WSA region.

Figure 13 shows the average of the zonal and meridional flows and the vertical velocity associated with the PE events. For type A subgroups, the zonal flows have the same eastward direction at the lower levels of the atmosphere and on both sides of the Andes. On the west flank, zonal flows over the Pacific Ocean intensify until reaching the highest peak in the WSA region. Over the highland region around 68°W, a significant flow of humidity is observed at levels above 4 km that goes from the adjacent slopes of the Amazon region towards the interior of the Andes. In addition, the southern flows (Fig. 13b) show an increase in their magnitude within the Andes and are directed towards the south. On the contrary, on the slopes of the WSA region the direction of the flows is towards the north.

In the case of type B subgroups, the low-level zonal flows are like those of type A, but there is an appreciable increase in the magnitude of the zonal flows between 4 and 8 km above the Pacific Ocean, while in the interior of the Andes there is a decrease in the magnitude of the zonal flows. In the same way, a decrease in the magnitude of the southern flows on the slopes of the WSA region is observed. Finally, for the subgroups of type C, the patterns of the zonal humidity fluxes change considerably in relation to the other subgroups, since a dominant pattern of the eastern flows from the Amazon is observed in the middle and high levels of the atmosphere that are associated with the occurrence of PE events. In addition, the southern moisture flows come exclusively from the south and are deeper reaching 8 km above the Pacific Ocean. For the three subgroups A, B, C, the vertical movements are intense and well localized, which shows that there is a consistent correlation with the positive anomalies of CAPE that favor deep convection (Fig. 7).

5 | DISCUSSION

Comparing the correlations between En and En* calculated here with those in [27], lower correlations are found in the WSA region. This is possibly due to the different physical mechanisms at work in tropical regions compared to mid-latitudes [29]. For example, the diurnal cycle of atmospheric variables and thermal circulations induce localized precipitation [19]. The effectiveness of indices (R and T) is associated with the moderate correlations between En and En*, where the T index explains 59% of the variance of precipitation in WSA, while the R index explains the remaining 41%.

From the pluviometric data it is necessary to select an adequate temporal scale to quantify the LGP patterns on the slopes of the Andes. On a daily scale, positive and negative LGP values have been found, which shows that there are precipitation events that produce greater accumulated precipitation in the lower parts (NG events) and other times in the upper parts (PG events) of the WSA. In the case of PEs, 80% of PEs have been found in NG-type events and 17% of PEs in PG events, showing that the R index has potential predictability to characterize precipitation variations in the region WSA. For this study region, the precipitation events characterized as negative LGP are of greater interest, since these events directly impact the low-lying areas of the Peru region (Arequipa, Moquegua and Tacna).

The detection of the NWMF and EMF flows were constructed based on the IVT calculated with the ERA5 reanalysis [25]. IVT plumes characterized as long and narrow corridors of strong water vapor transport are known as atmospheric rivers (AR) in mid-latitudes [30]. One of the criteria that [31] used to detect ARs is the 85th of the IVT in the atmospheric column (1000-100 hPa), while here we used the 80th of the IVT for two layers (650-200 hPa and 800-875 hPa). Additional thresholds (85th, 80th, 75th) were tested and the 80th percentile was more consistent and better associated with precipitation in the study area. The NWMF flow was exclusively detected over the Pacific Ocean, regardless of whether these flows passed through the WSA coastal region. Whereas the EMF flow was detected when it managed to move into the WSA (Fig. 2).

The predominance of NWMFs and EMFs were key to explaining the WSA precipitation patterns. The impacts of these flows vary annually. In addition, both flows regionally transport water vapor from both sides of the Andes, and the convergence of both flows explains the generation of intense precipitation in WSA and contributes significantly to the total accumulated precipitation [19, 32]. The highest fraction of precipitation above 80% is found for the summers of 2008, 2009, 2017 and 2019 in T1 and T2 (Figs. 11a and 11b). During these years, the SST anomaly was positive in the southeastern Pacific Ocean and there were strong NWMFs, thus providing moisture to the WSA. A key example is summer 2017, when an intense northerly wind anomaly occurred near the surface due to weak westerlies in the free troposphere along the north coast of Chile, in conjunction with warm SSTs in the southeastern Pacific [12, 33]. The NWMF in both transects is associated with a high fraction of the precipitation in WSA. This is mainly because NWMFs have a higher frequency of occurrence than EMFs (Fig. 10). The NWMF occurs 16 times per summer, and the EMF 10 times per summer. In the period 2000-2019, the EMF was observed 28% less than the NWMF which is associated with a lower probability for the formation of intense precipitation events.

The convergence of both NWMF and EMF is the main cause for the occurrence of PE events, because they condition the intensities of PE events in both transects of the WSA region. For example, when they occur simultaneously, they explain 51% of PE events in T1 and 58% of PE events in T2. From the local radiosonde observations, reanalysis data and SSTs, it was found that the atmospheric structure has specific characteristics in its dynamics and thermodynamics during the occurrence of PE events, which favor an increase in the precipitable water content over WSA and off the coastal (Fig. 7c). In Fig. 14 a conceptual diagram is proposed, where the atmospheric elements that control the PE events during summer are shown.

First, at levels close to the sea surface and parallel to the coast of Peru, there is an important ocean-atmosphere interaction at a local and regional scale [9]. The result of this interaction favors a local increase in water vapor at low atmospheric levels. Under these atmospheric conditions, there is a weakening of the southern winds in the eastern Pacific Ocean and local and regional warming off the coast of Peru [33]. One of the most obvious relationships that we find during the occurrence of PE events is that the south wind weakens in response to the geopotential height gradient anomaly and the sea warms up and then there is a local increase in the water vapor content. The warming of the sea is most likely responding to the weakening of the upwelling [12]. The effect of the ocean current has not been analyzed in this work. Thus, this is an open question to link PE events, upwelling, and Humboldt Current in greater depth with a regional approach. Our results are in agreement with the studies by [12]. Likewise, it is evident that the low-levels of the atmosphere has an important role on the SST [9, 34], whose anomaly, by itself, is not decisive for the increase in the precipitable water vapor content in the atmosphere (Fig. 7c). But it also depends on other factors, such as the circulation of the atmosphere at the surface, that favors the advection of water vapor in southern Peru [14, 12].

Second, at 875-800 hPa the NWMF intensifies over the Pacific Ocean as an atmospheric jet that carries warmer and more humid air from the north to the south of Peru. The atmospheric jet elongates closely off the coast of Peru and according to the classification of atmospheric phenomena on a horizontal scale. This jet is categorized as mesoscale-alpha type [35], because its duration is approximately one day and its spatial scale is around 1800 km. This regional connection, through the atmospheric jet, between the north and south of Peru is key during the occurrence of PE events. The variability of precipitation over the WSA region is largely explained by the NWMF and by the fluctuations of the SST, which together favor a higher availability of water vapor content in the climatologically dry WSA region [2, 3]. Northern flows at low levels of the troposphere (Fig. 10a) play an important role in the transport of water vapor along the Peruvian coast. The NWMF between 10° S and 15°S penetrates deeper towards the western slopes of the Andes and in association with the upslope winds, managed to surpass the Andes mountain range, producing intense events in the Central Andes of Peru [36]. In this study we reveal that the NWMF has an impact on precipitation between 15°S and 20°S on the western slopes of the Andes, it would be interesting to extend the analysis from 15°S to low latitudes to understand the flow impact on precipitation in the western slope of the Andes

Third, at 650-200 hPa the EMFs transport water vapor from the Amazon (east side of the Andes) over the WSA region. In particular, the magnitude of these flows intensifies (Fig. 9f) in the interior of the Andes due to diurnal effects in association with the synoptic circulation that predominate in this tropical region [19, 32]. At these levels, the atmosphere is warmer because it is strongly influenced by the position of the BH. For the PE events, it was found that the BH is very intense, and its geographic center is well defined, which favors the advection of water vapor from the Amazon towards the interior of the Andes [14]. These characteristics of the BH are similar for the intense precipitations that occur in the Altiplano of the central Andes [13, 16]. Likewise, it was found that an atmospheric blocking pattern occurs at these levels, since the eastern circulation weakens in response to an intense gradient of the geopotential height anomaly (Fig. 5 and 6). Coincidentally, this weakening of this circulation occurs over the WSA region, which favors the accumulation of precipitable water vapor over the same region.

The intensity and frequency of PE events are associated with the NWMF and EMF. When these flows occur simultaneously the PE events are more intense near the coast and on the lower slopes of the WSA region. This is due to the convergence of the zonal flows, which generates intense vertical speeds with a depth that exceeds 12 km in height. When this convergence occurs, rainfall is more intense in both T1 and T2. The greatest influence on precipitation in upper part of the WSA corresponds to the EMF in T1 as in T2. In addition, the intense vertical velocity was associated with an intense advection of water vapor from the eastern slopes of the Andes, most likely due to the intensification of thermal circulations [16, 37]. The NWMF and EMF have a regional scale effect with a daily scale frequency. Both flows were well identified, mainly for PE events. The NWMF has a tropical nature that transports water vapor from low latitude regions to high latitudes off the Peruvian coast.

6 | CONCLUSIONS

Summer rainfall associated with different transversal precipitation gradient types and precipitation extremes (PEs) over the western slopes of the Andes Mountains (WSA) was studied for the period of 2000-2019. Rain gauge data located along two transects (T1 and T2) were used to calculate two indices (R and T) using principal component analysis. The R index characterized the precipitation gradient over the WSA region and was used to classify positive (PG), negative (NG) and neutral (Neu) gradient events. PE events were classified using the 95th percentile of the study period.

The transversal rainfall in the WSA region was explained with a variance of 59% by the T index and 41% by the R index. The latter indicates that the precipitation gradient is important at a daily scale in the WSA. The PE and NG events are characterized by negative gradients in the WSA region. These events have a direct impact on the water system in coastal and low slope areas. At a distance of 70km from the coast of WSA, the 75th percentile is 9 mm/day and the maximum value is 30 mm/day, while the average is 2 mm/day. Due to the extreme intensity of precipitation that the PE events generate, they could significantly affect the hydraulic infrastructure in the departments of Peru (Arequipa, Moquegua and Tacna).

A significant fraction of the WSA precipitation is associated with the north-westerly moisture flow (NWMF) and easterly moisture flow (EMF). On average, 69% of the precipitation in T1 and 68% in T2 were associated with NWMFs. For summer 2017 the fraction of precipitation exceeded 90% in both transects. Meanwhile, 58% of the precipitation in T1 and 59% in T2 were associated with EMFs. On average, 82% of PE events were associated with NWMFs and 68% were associated with EMFs. These results imply that both NWMF and EMF play an important role in generating rainfall over WSA, especially for PE events.

Precipitable water was concentrated over WSA and its coastal zone, forming a well-defined hot-spot of moisture during PE events. The formation of this hot-spot depends on various atmospheric mechanisms and SST fluctuations over the eastern Pacific Ocean. The atmospheric configuration is as follows:

- Near the surface, southerly flows weakened and Pacific Ocean SSTs increased, which favored an increase in moisture content off the coast of WSA.
- From 875-800 hPa, the NWMF flow intensified over the Pacific Ocean. This alpha-type mesoscale flow acted as a water vapor corridor, reaching the north of Chile (23°C)
- At 500-200 hPa, EMF flows were responsible for transporting moisture from the Amazon to the eastern side of the Andes. An atmospheric blocking pattern sets up north of Chile, favoring the persistence of the precipitable water hot-spot.

PE events had high CAPE values compared to NG and PG events, with CAPE developing mainly on the slopes of the WSA. In turn, these events presented intense and deep vertical velocities reaching over 12 km high. With these atmospheric conditions, PE events occurred mostly in February (56%) and January (39%) in T1, and 46% of PE events occurred in both months for T2. These results suggest that the atmosphere of southern Peru can become extremely unstable, favoring the development of intense convection that causes extreme rainfall events in WSA.

acknowledgements

The processing of the reanalysis data was done using computational resources from the HPC-Linux Cluster from Laboratorio de Dinamica de Fluidos Geofisicos Computacionales of Instituto Geofísico del Perú (IGP) (grant 101-2014-FONDECYT, SPIRALES2012 IRD-IGP, Manglares IGPIDRC, PpR068). Thanks to National Service of Meteorology and Hydrology of Peru (SENAMHI) for the rain gauge precipitation data.

conflict of interest

The authors declare that they have no conflict of interest: This work is a part of the auhtor's Ph.D. thesis titled 'Procesos físicos que controlan la precipitación orográfica en los Andes tropicales de Perú', doctoral program in water resources of Universidad Nacional Agraria La Molina

references

[1] Espinoza JC, Chavez S, Ronchail J, Junquas C, Takahashi K, Lavado W. Rainfall hotspots over the southern tropical Andes: Spatial distribution, rainfall intensity, and relations with large-scale atmospheric circulation. Water Resources Research 2015;51(5):3459–3475.

[2] Rau P, Bourrel L, Labat D, Melo P, Dewitte B, Frappart F, et al. Regionalization of rainfall over the Peruvian Pacific slope and coast. International Journal of Climatology 2017;37(1):143–158.

[3] Trachte K, Seidel J, Figueroa R, Otto M, Bendix J. Cross-scale precipitation variability in a semiarid catchment area on the western slopes of the central andes. Journal of Applied Meteorology and Climatology 2018;57(3):675–694.

[4] Lagos P, Silva Y, Nickl E, Mosquera K. El Niño–related precipitation variability in Perú. Advances in Geosciences 2008;14:231–237.

[5] Lavado Casimiro WS, Labat D, Ronchail J, Espinoza JC, Guyot JL. Trends in rainfall and temperature in the Peruvian Amazon–Andes basin over the last 40 years (1965–2007). Hydrological Processes 2013;27(20):2944–2957.

[6] Bourrel L, Rau P, Dewitte B, Labat D, Lavado W, Coutaud A, et al. Low-frequency modulation and trend of the relationship between ENSO and precipitation along the northern to centre Peruvian Pacific coast. Hydrological processes 2015;29(6):1252–1266.

[7] Sulca J, Takahashi K, Espinoza JC, Vuille M, Lavado-Casimiro W. Impacts of different ENSO flavors and tropical Pacific convection variability (ITCZ, SPCZ) on austral summer rainfall in South America, with a focus on Peru. International Journal of Climatology 2018;38(1):420–435.

[8] Garreaud R. The Andes climate and weather. Advances in Geosciences 2009;22:3–11.

[9] Takahashi K, Battisti DS. Processes controlling the mean tropical Pacific precipitation pattern. Part I: The Andes and the eastern Pacific ITCZ. Journal of Climate 2007;20(14):3434–3451.

[10] Dewitte B, Illig S, Renault L, Goubanova K, Takahashi K, Gushchina D, et al. Modes of covariability between sea surface temperature and wind stress intraseasonal anomalies along the coast of Peru from satellite observations (2000–2008). Journal of Geophysical Research: Oceans 2011;116(C4).

[11] Rahn DA, Garreaud RD. A synoptic climatology of the near-surface wind along the west coast of South America. International Journal of Climatology 2014;34(3):780–792.

[12] Garreaud RD. A plausible atmospheric trigger for the 2017 coastal El Niño. International Journal of Climatology 2018;38:e1296–e1302.

[13] Garreaud R, Vuille M, Clement AC. The climate of the Altiplano: observed current conditions and mechanisms of past changes. Palaeogeography, palaeoclimatology, palaeoecology 2003;194(1-3):5–22.

[14] Falvey M, Garreaud RD. Moisture variability over the South American Altiplano during the South American low level jet experiment (SALLJEX) observing season. Journal of Geophysical Research: Atmospheres 2005;110(D22).

[15] Lenters J, Cook KH. On the origin of the Bolivian high and related circulation features of the South American climate. Journal of the Atmospheric Sciences 1997;54(5):656–678.

[16] Vuille M, Keimig F. Interannual variability of summertime convective cloudiness and precipitation in the central Andes derived from ISCCP-B3 data. Journal of Climate 2004;17(17):3334–3348.

[17] Segura H, Espinoza JC, Junquas C, Lebel T, Vuille M, Garreaud R. Recent changes in the precipitation-driving processes over the southern tropical Andes/western Amazon. Climate Dynamics 2020;p. 1–19.

[18] Wang XY, Li X, Zhu J, Tanajura CA. The strengthening of Amazonian precipitation during the wet season driven by tropical sea surface temperature forcing. Environmental Research Letters 2018;13(9):094015.

[19] Junquas C, Takahashi K, Condom T, Espinoza JC, Chávez S, Sicart JE, et al. Understanding the influence of orography on the precipitation diurnal cycle and the associated atmospheric processes in the central Andes. Climate dynamics 2018;50(11):3995–4017.

[20] Segura H, Junquas C, Espinoza JC, Vuille M, Jauregui YR, Rabatel A, et al. New insights into the rainfall variability in the tropical Andes on seasonal and interannual time scales. Climate dynamics 2019;53(1):405–426.

[21] Marengo JA, Soares WR, Saulo C, Nicolini M. Climatology of the low-level jet east of the Andes as derived from the NCEP–NCAR reanalyses: Characteristics and temporal variability. Journal of climate 2004;17(12):2261–2280.

[22] Lavado Casimiro WS, Ronchail J, Labat D, Espinoza JC, Guyot JL. Basin-scale analysis of rainfall and runoff in Peru (1969–2004): Pacific, Titicaca and Amazonas drainages. Hydrological Sciences Journal 2012;57(4):625–642.

[23] Chavez SP, Takahashi K. Orographic rainfall hot spots in the Andes-Amazon transition according to the TRMM precipitation radar and in situ data. Journal of Geophysical Research: Atmospheres 2017;122(11):5870–5882.

[24] Donlon CJ, Martin M, Stark J, Roberts-Jones J, Fiedler E, Wimmer W. The operational sea surface temperature and sea ice analysis (OSTIA) system. Remote Sensing of Environment 2012;116:140–158.

[25] Hersbach H, Bell B, Berrisford P, Hirahara S, Horányi A, Muñoz-Sabater J, et al. The ERA5 global reanalysis. Quarterly Journal of the Royal Meteorological Society 2020;146(730):1999–2049.

[26] Meukaleuni C, Lenouo A, Monkam D. Climatology of convective available potential energy (CAPE) in ERA-Interim reanalysis over West Africa. Atmospheric Science Letters 2016;17(1):65–70.

[27] Siler N, Roe G, Durran D. On the dynamical causes of variability in the rain-shadow effect: A case study of the Washington Cascades. Journal of Hydrometeorology 2013;14(1):122–139.

[28] Giovannettone JP, Barros AP. Probing regional orographic controls of precipitation and cloudiness in the central Andes using satellite data. Journal of Hydrometeorology 2009;10(1):167–182.

[29] Smith RB, Schafer P, Kirshbaum DJ, Regina E. Orographic precipitation in the tropics: Experiments in Dominica. Journal of Atmospheric Sciences 2009;66(6):1698–1716.

[30] Ralph FM, Dettinger MD, Cairns MM, Galarneau TJ, Eylander J. Defining atmospheric river: How the Glossary of Meteorology helped resolve a debate. Bulletin of the American Meteorological Society 2018;99(4):837–839.

[31] Viale M, Valenzuela R, Garreaud RD, Ralph FM. Impacts of atmospheric rivers on precipitation in southern South America. Journal of Hydrometeorology 2018;19(10):1671–1687.

[32] Flores Rojas J, AS MA, et al. Analysis of possible triggering mechanisms of severe thunderstorms in the tropical central Andes of Peru, Mantaro Valley. Atmosphere 2019;10(6):301.

[33] Son R, Wang SYS, Tseng WL, Schuler CWB, Becker E, Yoon JH. Climate diagnostics of the extreme floods in Peru during early 2017. Climate Dynamics 2020;54(1):935–945.

[34] Illig S, Dewitte B, Goubanova K, Cambon G, Boucharel J, Monetti F, et al. Forcing mechanisms of intraseasonal SST variability off central Peru in 2000–2008. Journal of Geophysical Research: Oceans 2014;119(6):3548–3573.

[35] Orlanski I. A rational subdivision of scales for atmospheric processes. Bulletin of the American Meteorological Society 1975;p. 527–530.

[36] Flores-Rojas JL, Moya-Alvarez AS, Valdivia-Prado JM, Piñas-Laura M, Kumar S, Abi Karam H, et al. On the dynamic mechanisms of intense rainfall events in the central Andes of Peru, Mantaro valley. Atmospheric Research 2021;248:105188.

[37] Vera CS, Díaz LB, Saurral RI. Influence of anthropogenically-forced global warming and natural climate variability in the rainfall changes observed over the south American Altiplano. Frontiers in Environmental Science 2019;7:87.

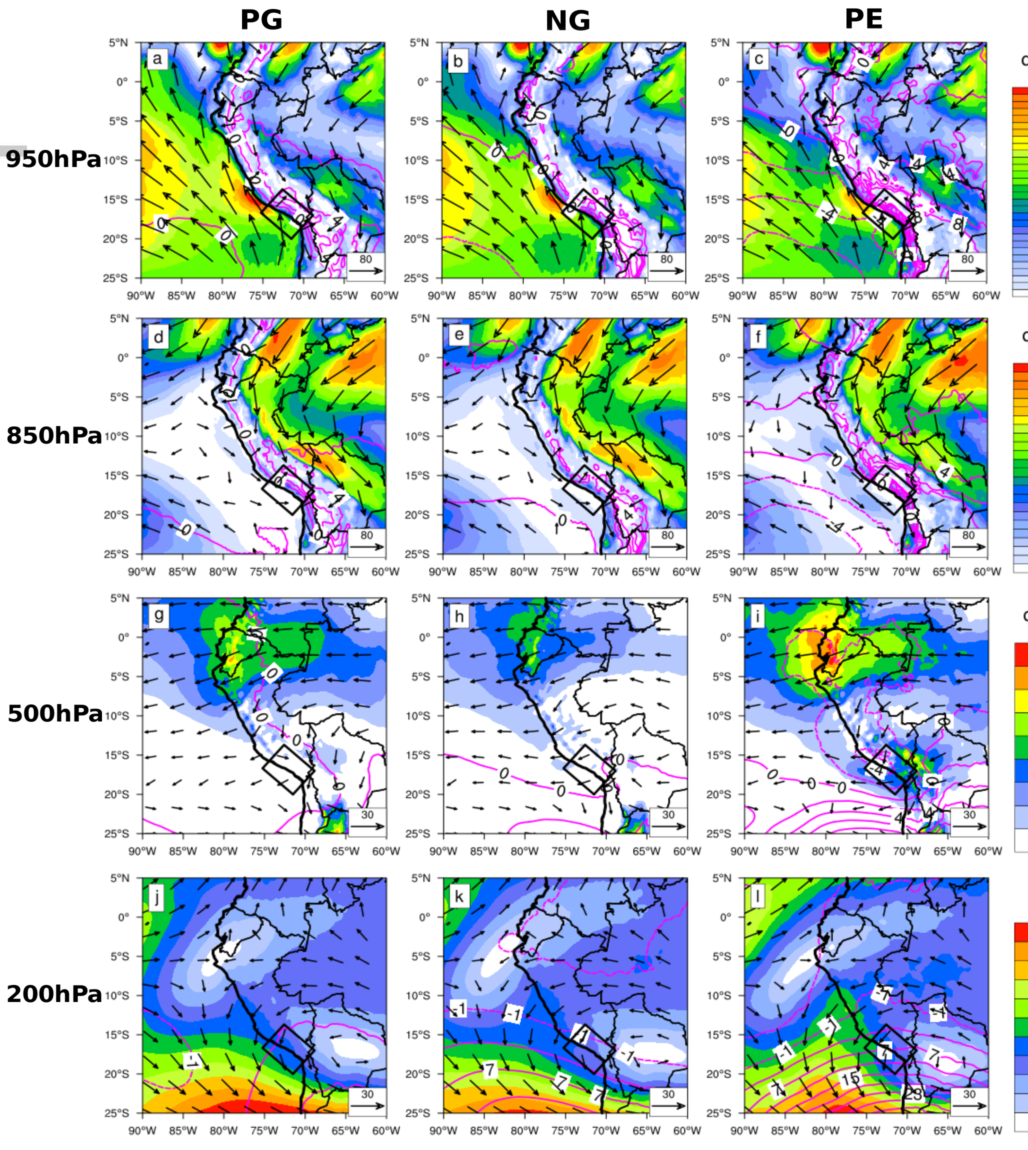

FIGURE 5 Panels a to i show average moisture transport of vapor water (qU, g/kg*m/s) (shaded), and panels j to l show average horizontal wind speed (U, m/s). Geopotential height anomalies relative to the climatology (magenta contours at 2 m intervals for panels a to i and 4 m intervals for panels j to l) are shown for different pressure levels: 950-hPa, 850-hPa, 500-hPa and 200-hPa associated with PG, NG and PE events. The black box denotes the WSA region.

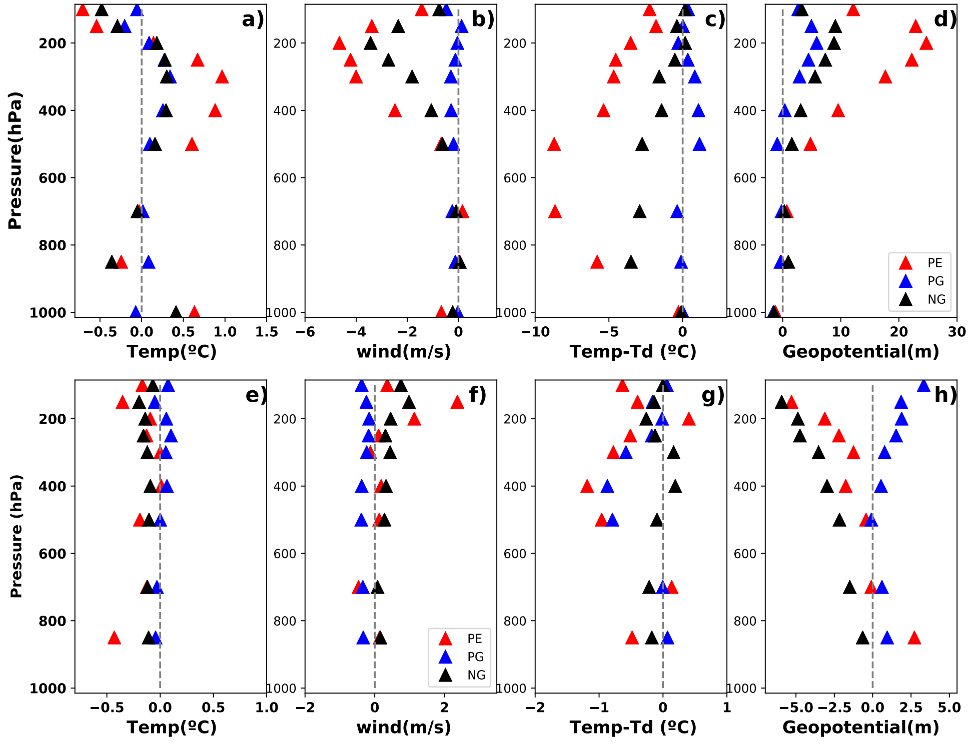

FIGURE 6 Vertical profiles of anomalies from radiosondes. The upper panels (a, b, c, d) correspond to the radiosondes at Antofagasta (Chile); a) temperature anomaly (°C), b) horizontal wind anomaly (m/s), c) dew point depression anomaly (Temp-Td), d) geopotential height anomaly (m). Lower panels (e, f, g, h) are the same as the upper panels, but for radiosondes from Rio Branco (Brazil). In Rio Branco (Antofagasta), 57 (74), 312 (473) and 354 (476) observations were found for PE (red triangles), PG (blue triangles) and NG (black triangles) type events, respectively.

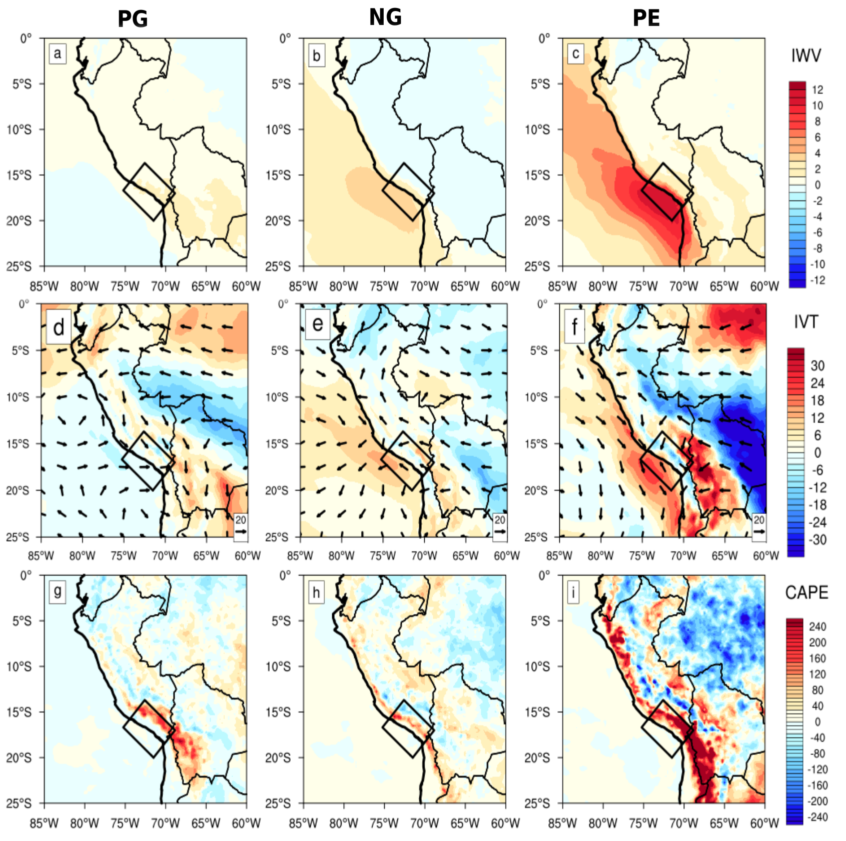

FIGURE 7 Anomalies of atmospheric variables associated with each group of precipitation PG, NG and PE using the 2000-2019 data series. a), b) and c) are IWV anomalies (kg/m^2), d), e) and i) are IVT anomalies (kg/m^{1}s^1), where the IVT were integrated over levels 975-200 hPa and the wind arrows are anomalies of the IVT vector. g), h) and i) are CAPE anomalies (J/kg). The black box denotes the WSA region.

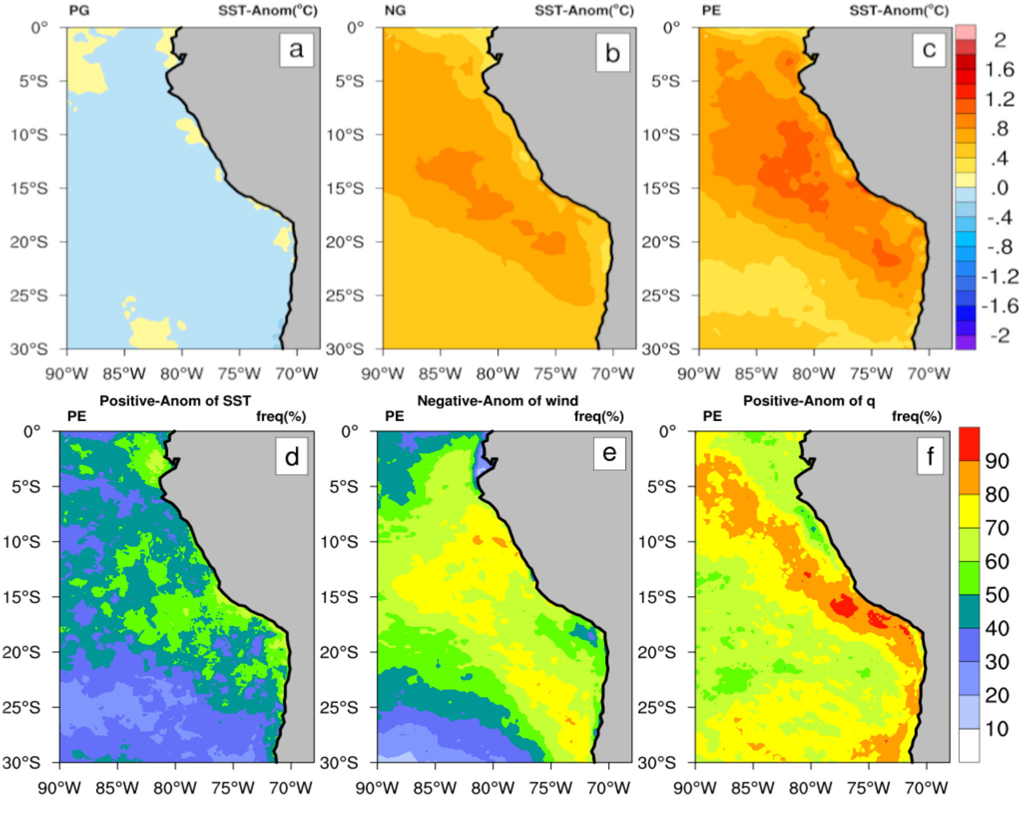

FIGURE 8 Upper panels are sea surface temperature (SST) anomalies associated with precipitation events a) PG, b) NG and c) PE. Lower panels are frequency anomalies (%) of occurrence associated with events PE (54), d) frequency of positive anomaly of the SST, e) frequency of negative horizontal wind anomaly and f) frequency of positive anomaly of humidity , the last two (wind and humidity) were calculated at 975-hPa.

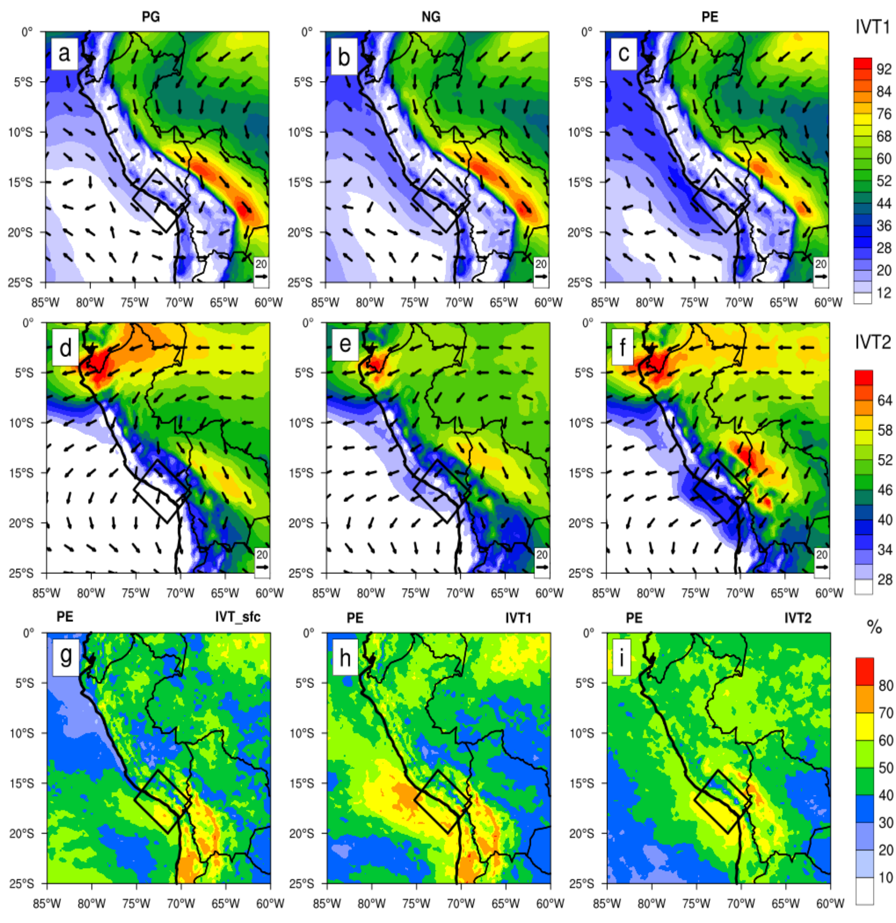

FIGURE 9 IVTs and its frequency in different layers of the atmosphere; a), b) and c) IVT1 (integrated in the 875-800 hPa levels) associated with the PG, NG and PE events, respectively. d), e) and f) IVT2 (integrated in levels 650-200 hPa) associated with the PG, NG and PE events, respectively. g), h) and i) are frequencies (%) of occurrence of the positive anomaly of the IVTs (IVT_sfc, IVT1 and IVT2) only for the PE events, the IVT_sfc is integrated in the levels 975-950 hPa.

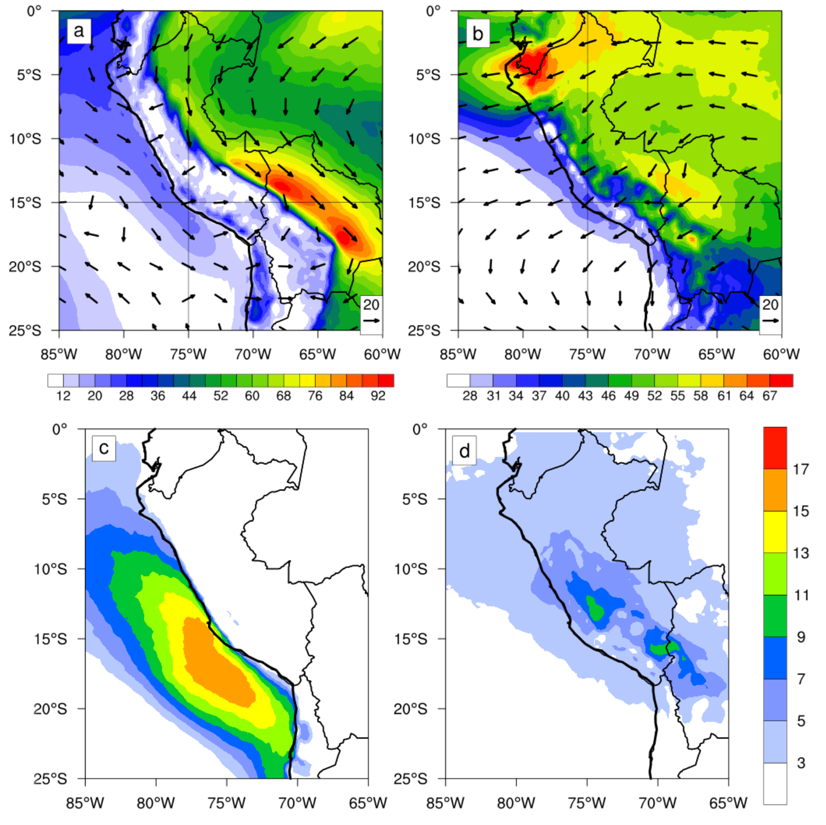

FIGURE 10 Average flows (NWMF and EMF) identified in the period 2000-2019 using the flow detection algorithm, a) NWMF flow and b) EMF flow (colorbars have different scales). Summer frequency (average number of flows) are c) NWMF flow and d) EMF flow.

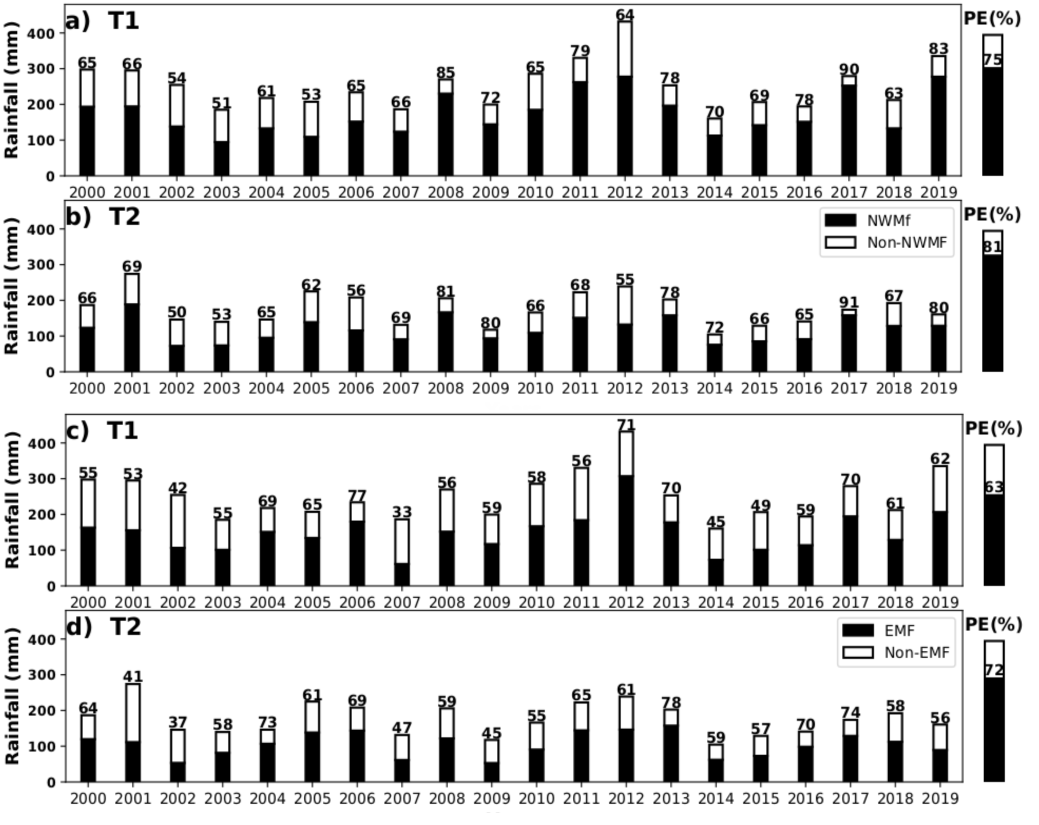

FIGURE 11 Fraction of precipitation (%, numbers above each bar) associated with the NWMF and EMF determined in each summer during the period 2000-2019. a) T1 transect and b) T2 transect both associated with the NWMF, c) T1 transect and d) T2 transect both associated with the EMF flow. PE(%) indicates the percentage of extreme events that explains the NWMF and EMF in each transect.

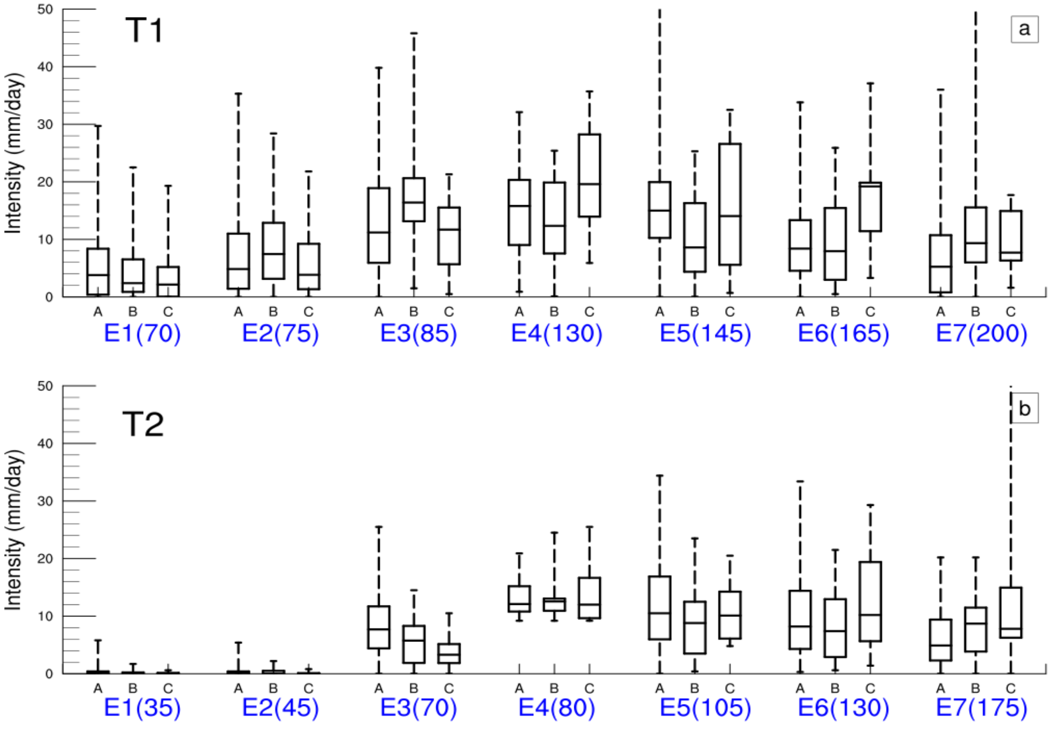

FIGURE 12 Rain intensity (mm/day) of type PE associated with flows of type A, B and C, where E1, E2, E3, ..., E7 (blue color) are the rainfall stations and their respective position in km (indicated in parenthesis). a) T1 transect and b) T2 transect. The boxplot was built based on the minimum and maximum, and 25th, 50th and 75th percentiles.

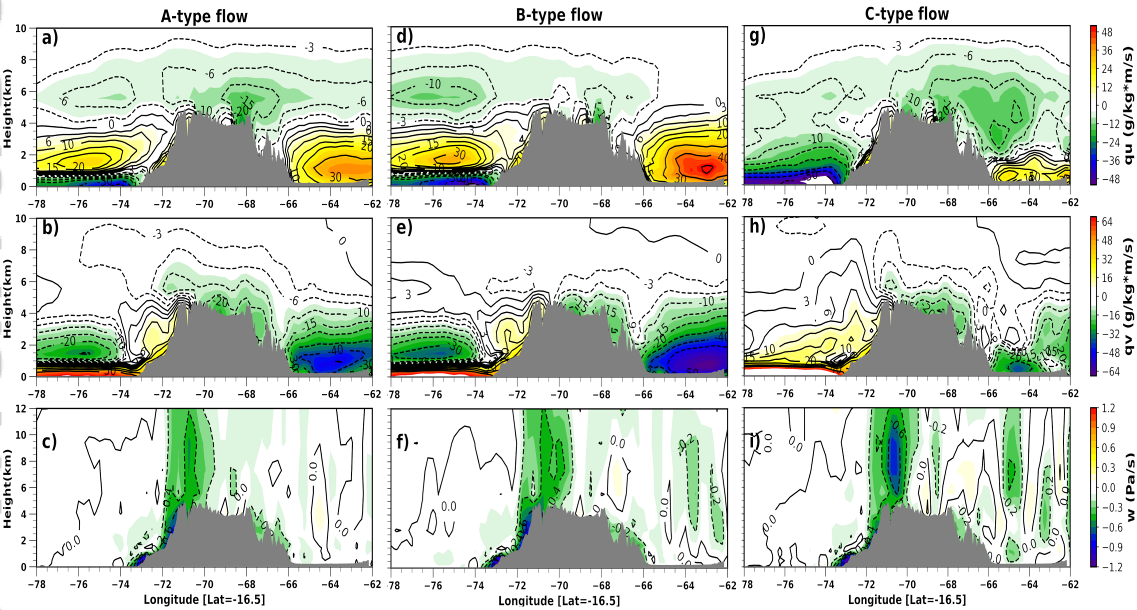

FIGURE 13 Composition of zonal and meridional flows and the vertical velocity associated with types of flows A, B and C. a) zonal flow (u*q) of type A, b) meridional flow (v*q) of type A, c) vertical velocity (Pa*s^{-1}) of type A. d), e) and f) is like the left column, but, for flow of type B, g), h) and i) is like the left column, but, for type C flow.

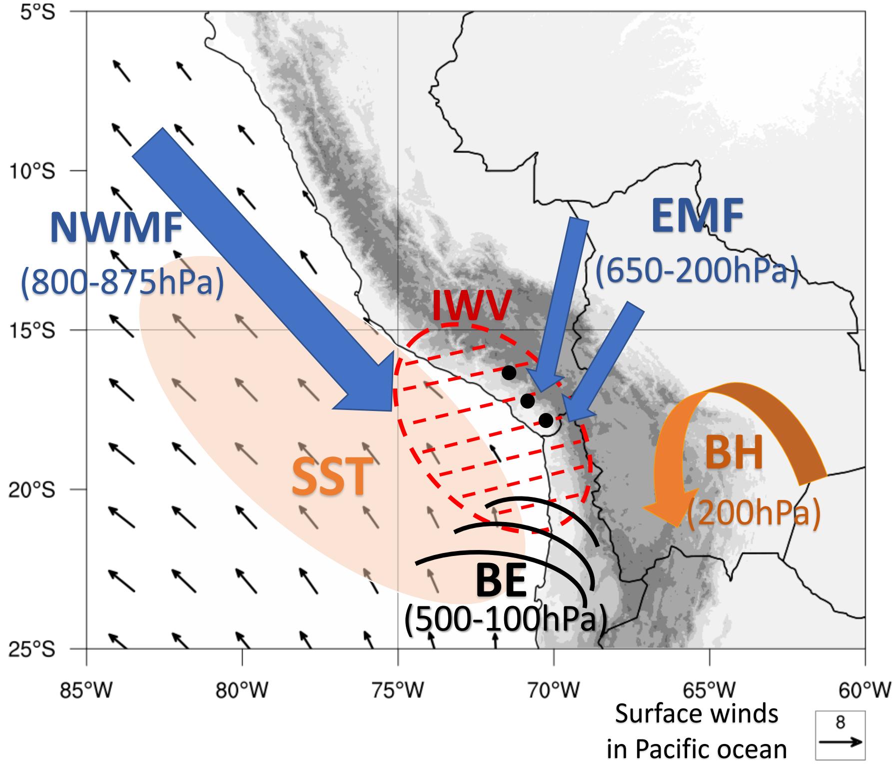

FIGURE 14 Schematic representation of the atmospheric mechanisms controlling to the PE events during the summer (December-February) on WSA region. For the PE events it generates a high concentration of the integrated water vapor in the vertical column (IWV) on WSA region and its coast. This well-defined hot-spot region of IWV depends on the following settings: There is a weakening of the south winds at levels close to the sea surface and regional warming of the sea (SST, sea surface temperature). At levels of 800-875 hPa the Northwesterly Moisture flow (NWMF) intensifies as a water vapor corridor along the Peruvian coast. At levels of 500-100 hPa it generates an atmospheric blocking effect (BE), and at levels of 650-200 hPa the Easterly Moisture Flow (EMF) moisture transport from the Amazon and this flow accompanied by an intense Bolivian High (BH, 200 hPa) introduces moisture on WSA region and its coast. Black dots from north to south are Arequipa, Moquegua and Tacna, respectively.